Supplementary Information

# Achieving High Power and Low Crest Factor of Direct-Current Triboelectric Nanogenerator for Self-Powered Optical Computing System

Hongyun Li,†[a] Shaobo Lv,†[a] Binbin Zhang,[b] Bochao Liu,[c] Jin Yang,[c] Hengyu Guo,[c] Yiyuan Xie,*[a] and Zhiming Lin*[a]

*a. School of Electronics and Information Engineering, Southwest University, Chongqing 400715, P. R. China.*

*b. Department of Biomedical Engineering, City University of Hong Kong, Hong Kong, China.*

*c. Department of Optoelectronic Engineering, Key Laboratory of Optoelectronic Technology and Systems, Ministry of Education, Chongqing University, Chongqing 400044, P. R. China.*

† These authors contributed equally to this work.

* Correspondence: zhiminglin@swu.edu.cn

‡ Electronic Supplementary Information (ESI) available

See DOI: 10.1039/x0xx00000x

# Supplementary Figures:

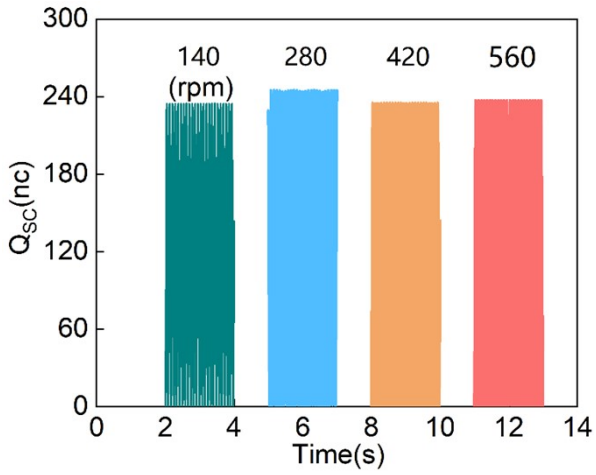


**Figure. S1** | The transferred charges of the single-phase output of 4P6G D-TENG at different speeds.

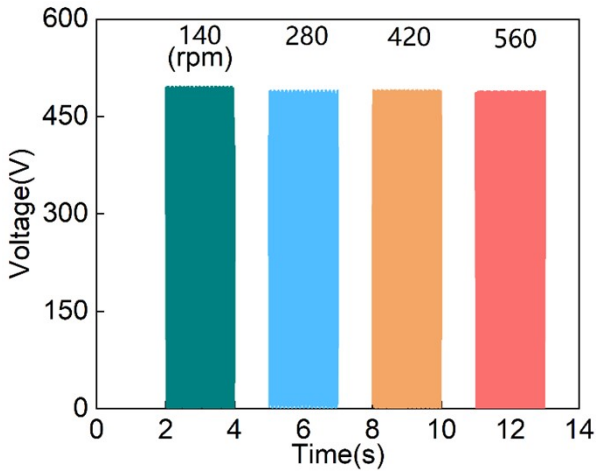


**Figure. S2** | The output voltages of the single-phase output of 4P6G D-TENG at different speeds.

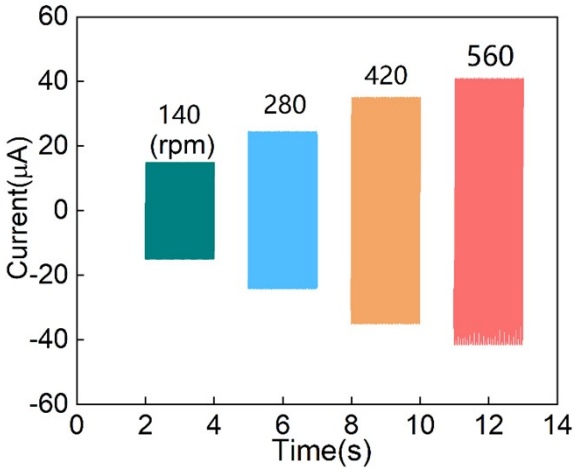


**Figure. S3** | The output currents of the single-phase output of 4P6G D-TENG at different speeds.

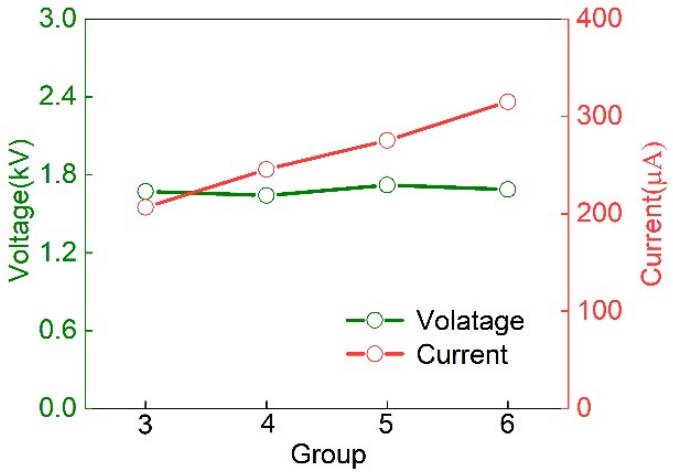


**Figure. S4** | The voltages and currents of the single-phase output of 1P3G, 1P4G, 1P5G, and 1P6G D-TENG at 560rpm.

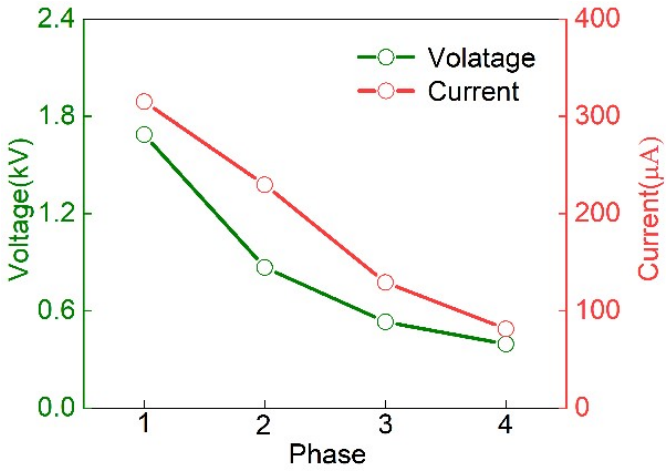


**Figure. S5** | The voltages and currents of the single-phase output of 1P6G, 2P6G, 3P6G, and 4P6G D-TENG at 560rpm.

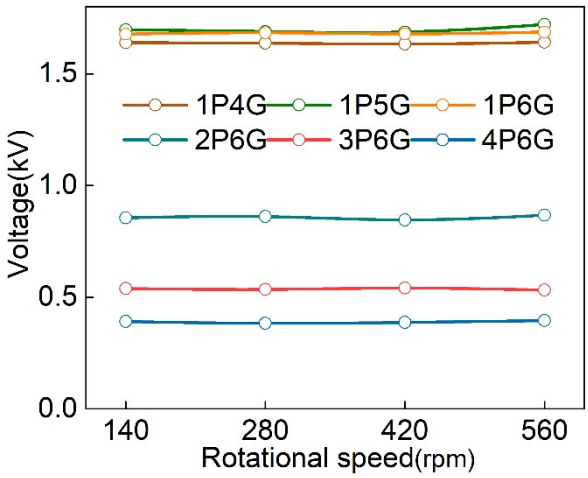


**Figure. S6** | The voltages of the single-phase output of D-TENGs at different speeds.

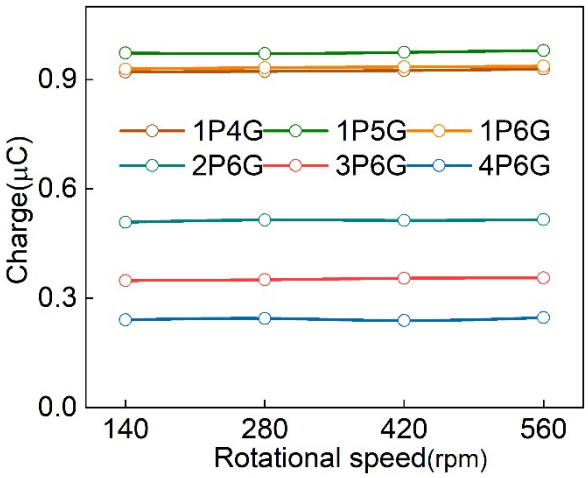


**Figure. S7** | The transferred charges of the single-phase output of D-TENGs at different speeds.

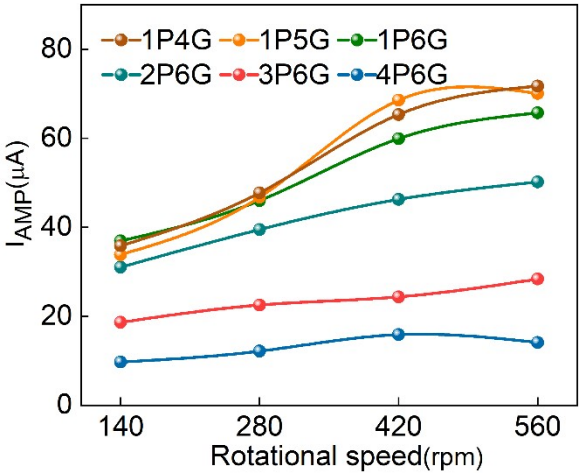


**Figure. S8** | The current amplitude of diverse D-TENG.

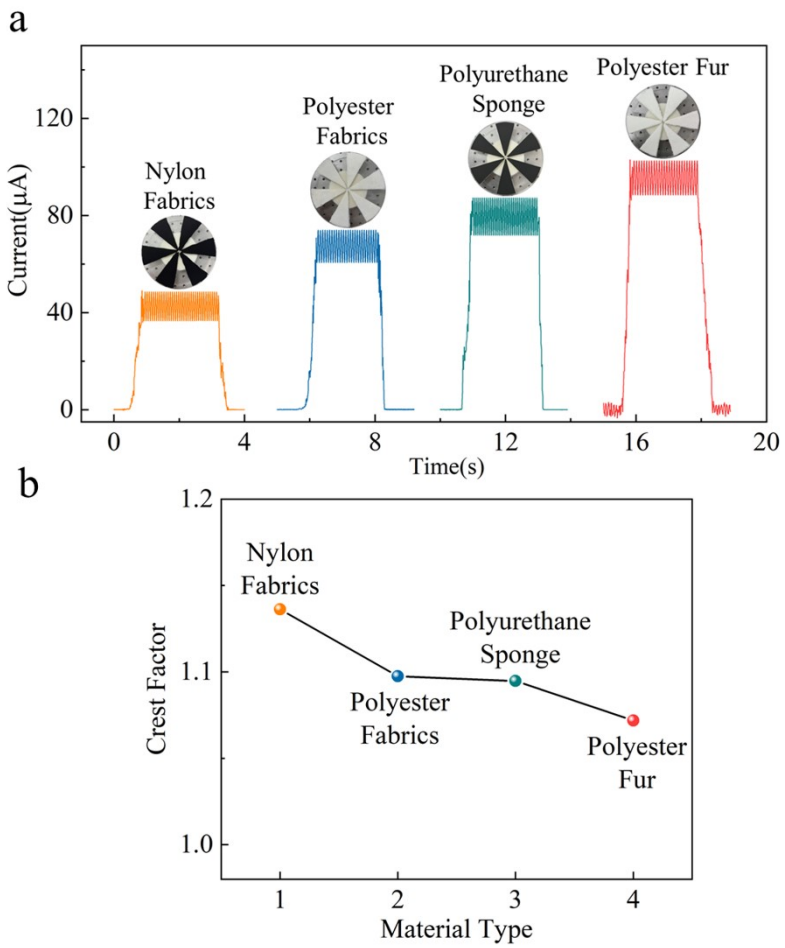


**Figure. S9** | (a) Coupling currents and (b) crest factor of the 4P6G D-TENG with different common materials (nylon fabrics, polyester fabrics, polyurethane sponge, and polyester fur) as rotators.

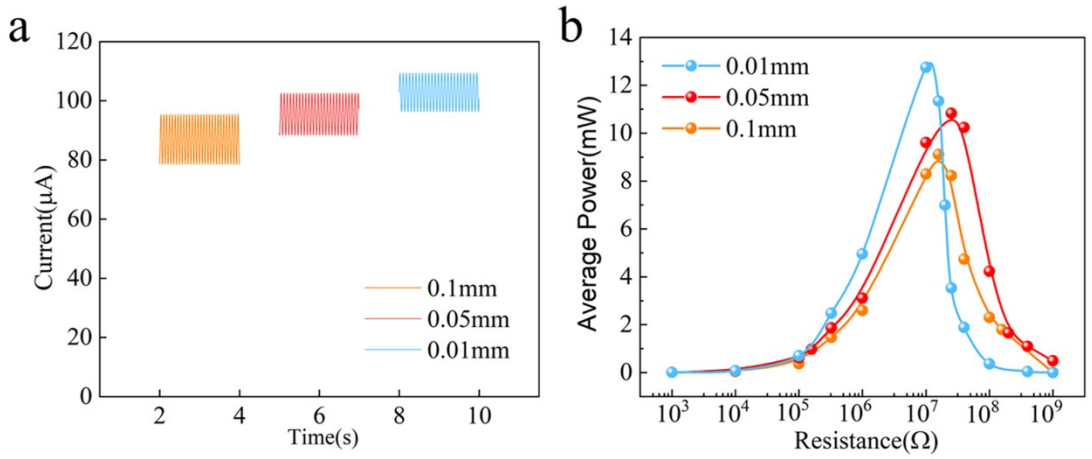


**Figure. S10** | (a) Coupling currents and (b) average power of D-TENG with different thickness of FEP films.

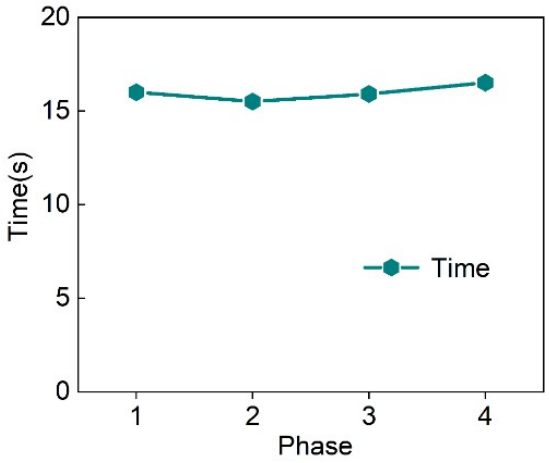


**Figure. S11** | Characterization of each phase for 4P6G D-TENG to charge a same capacitor (1.1mF).

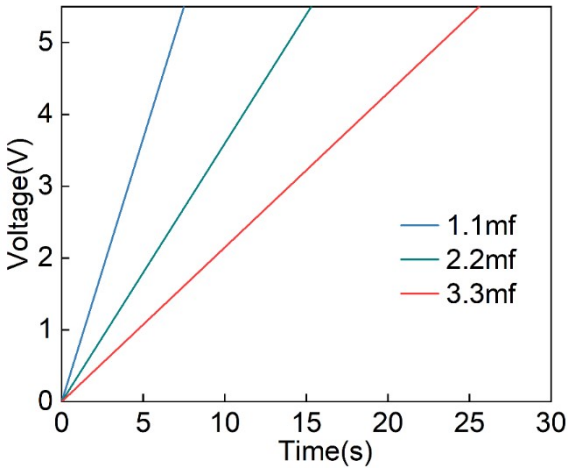


**Figure. S12** | Charging characteristics of D-TENG for different capacitors.

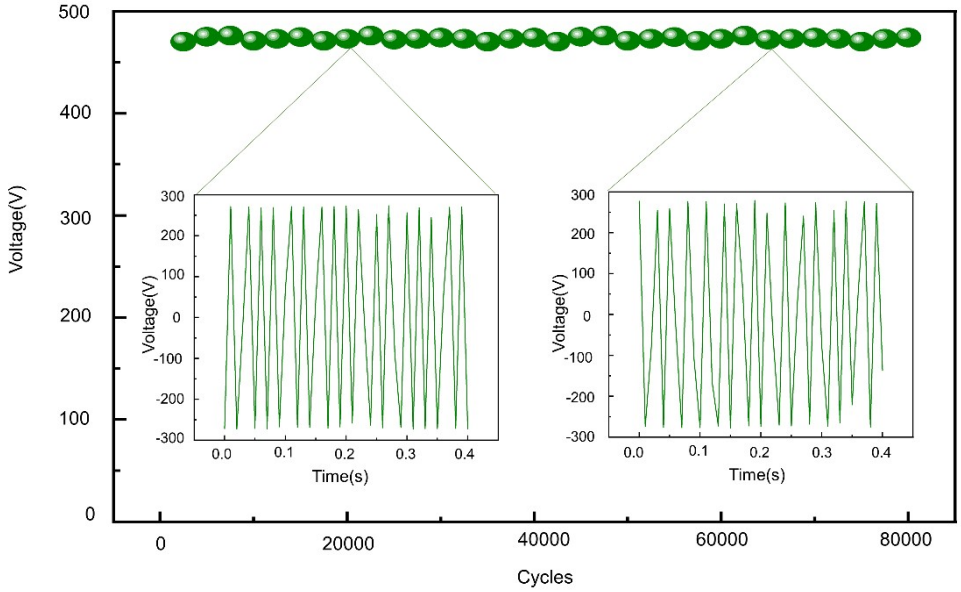


**Figure. S13** | Durability test of the D-TENG over 80,000 working cycles.

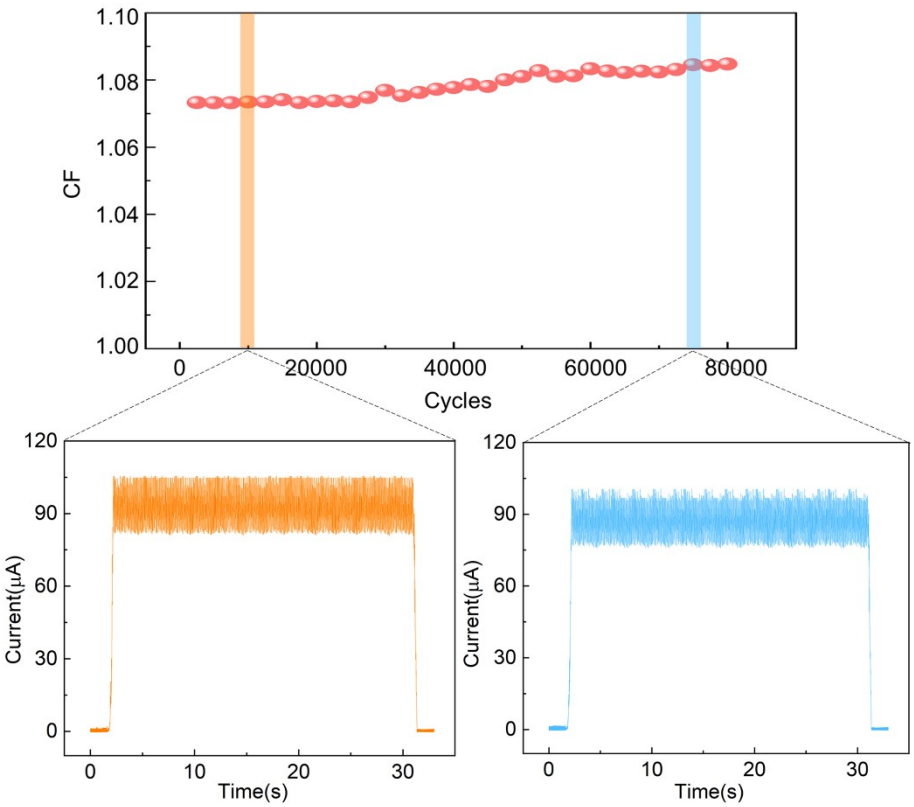


**Figure. S14** | The output coupling current and crest factor for long-term operation.

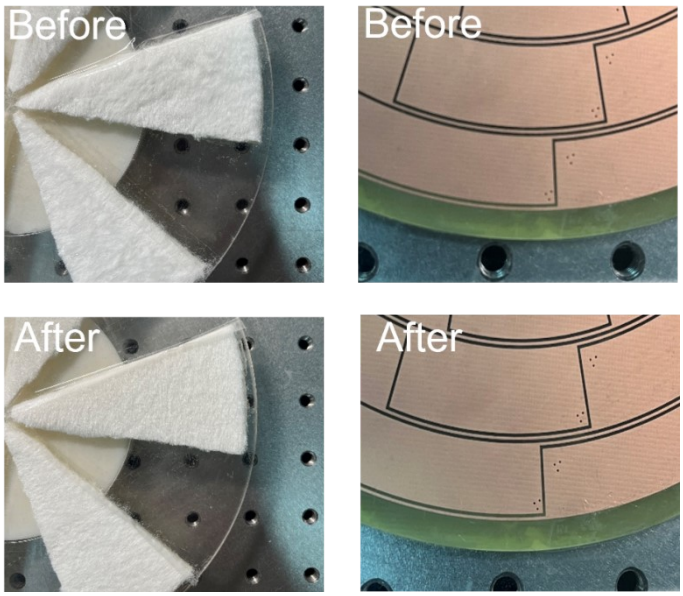


**Figure. S15** | Before and after the stability test of the fur and the FEP film.

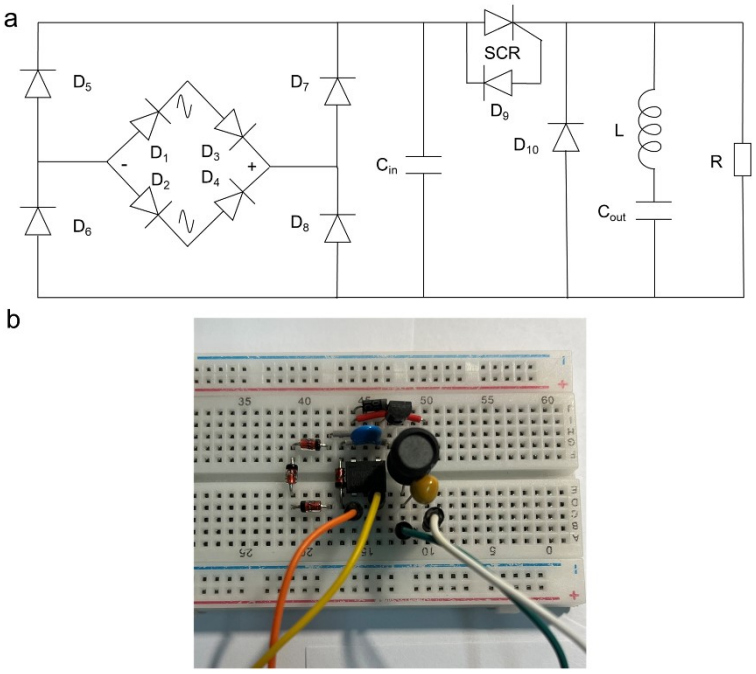


**Figure. S16** | (a) Specific circuit of PMC, (b) Photograph of the PMC.

# Supplementary Table:

**Table. S1** | The comparison of different working mechanisms of DC-TENGs.

| DC-TENG | Working mechanism | Advantages | Disadvantages |
|---|---|---|---|
| **Electrostatic Breakdown** | Coupling of triboelectrification and electrostatic breakdown | Effective use of air breakdown; High output power density | Complex fabrication; Material wear |
| **Tribovoltaic Effect** | Electron hole pairs driven by built-in electric field | High current density; Simple structure design | Low output voltage; Material damage |
| **Phase Shift** | Multiphase coupling of parallel TNEG units | Low crest factor; High output | Complex design; Surface abrasion |

**Table. S2 |** Table of diverse designs depending on the phase difference.

| | **θ1** | **θ2** | **θ3** | **θ4** |
|---|---|---|---|---|
| **1P5G** | 0° | N/A[a)] | N/A[a)] | N/A[a)] |
| **1P6G** | 0° | N/A[a)] | N/A[a)] | N/A[a)] |
| **2P6G** | 0° | 15° | N/A[a)] | N/A[a)] |
| **3P6G** | 0° | 10° | 20° | N/A[a)] |
| **4P6G** | 0° | 7.5° | 15° | 22.5° |

**Table. S3** | The comparisons of the D-TENGs with different dielectric films.

| Dielectric materials | Open-circuit voltage (V) | Short-circuit current (uA) | Transferred charge (nC) | Crest factor |
|---|---|---|---|---|
| **FEP** | 473.48 | 35.97 | 240.56 | 1.073 |
| **Kapton** | 458.87 | 31.29 | 227.62 | 1.080 |
| **DuraLar polyester** | 447.56 | 29.67 | 217.57 | 1.087 |
| **Polyvinylidene fluoride** | 438.46 | 28.03 | 210.68 | 1.096 |

**Table. S4** | The performance of TENG in this work compared with others based on phase difference design.

| Structure | Size | Rotation speed (rpm) | Crest factor | Average power | Reference |
|---|---|---|---|---|---|
| 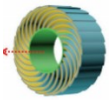 | 508.7 $cm^3$ | 480 | 1.31 | 4.4 ($W \cdot m^{-3}$) | 1 |
| 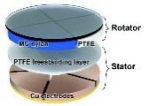 | 78.5 $cm^2$ | 918 | 1.26 | 40.6 ($mW \cdot m^{-2}$) | 2 |
| 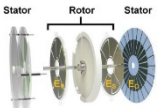 | 490.86 $cm^2$ | 300 | 1.23 | 187.02 ($mW \cdot m^{-2}$) | 3 |
| 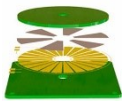 | 19.6 $cm^2$ | 750 | 1.09 | 98 ($mW \cdot m^{-2}$) | 4 |
|  | 226.0 $cm^2$ | 600 | 1.08 | 90.27 ($mW \cdot m^{-2}$) | 5 |
|  | 911.035 $cm^2$ | 240 | 1.07 | 120.74 ($mW \cdot m^{-2}$) | 6 |
| 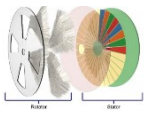 | 113.04 $cm^2$ | 300 | 1.05 | 271 ($mW \cdot m^{-2}$) | 7 |
|  | 1496.23 $cm^3$ | 500 | 1.05 | 10 ($W \cdot m^{-3}$) | 8 |
| 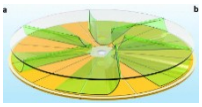 | 706.5 $cm^2$ | 480 | 1.03 | 254 ($mW \cdot m^{-2}$) | 9 |
| 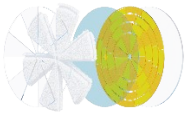 | 268.96 $cm^2$ | 560 | 1.07 | 385.93 ($mW \cdot m^{-2}$) | This work |

# Supplementary Notes:

**Note S1** | The definition and calculation of the phase difference.

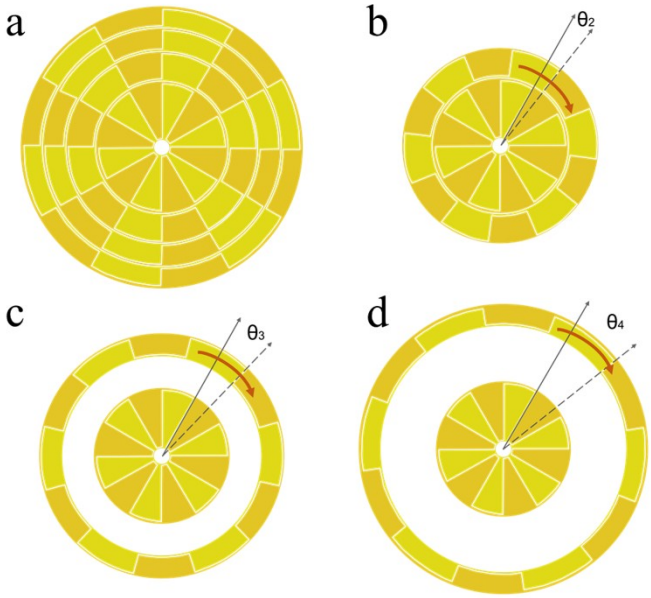


**Figure. S17** | Schematic diagram of phase shift process for the 4P6G D-TENG. (a) There is no phase difference between each phase. Schematic diagram phase shift process (b) Phase-2, (c) Phase-3, and (d) Phase-4, respectively.

On the basis of equal effective area for every phase, the phase difference depends on the number of groups and phases in the device. Figure S17 demonstrates the phase shift process for the 4P6G D-TENG, it could be found that the angle for every phase should be divided into 4 sections with equal angle to maintain the same interval of the outputs among the phases. Therefore, the equal phase difference $\theta$ between adjacent phases can be calculated as

$$\theta = \frac{360°}{N \cdot G \cdot P} \tag{1}$$

where $N$ is the number of electrodes per group (N = 2), $G$ is the number of groups per electrode ($G$ = 3, 4, 5, 6…), and $P$ is the number of phases ($P$ = 1, 2, 3, 4…). The phase difference $\theta_{n-m}$ between two phases can be determined by

$$\theta_{n-m} = (n-m) \cdot \theta, n \geq m \geq 1 \tag{2}$$

where $m$ and $n$ are the phase numbers, respectively.

**Note S2** | The detailed area design for 4P6G D-TENG.

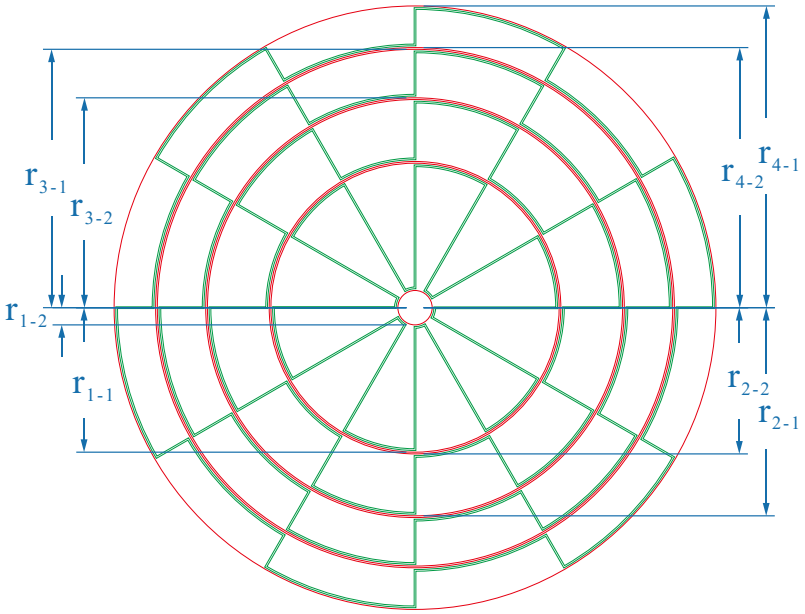


**Figure. S18** | Schematic diagram of the radius corresponding to each phase.

The detailed design process (4P6G D-TENG) is shown in Figure S18. Take away the areas of gap for each phase, the remaining area is divided into four same effective areas, which can be expressed as:

$$S_1 = \pi \cdot \left(r_{1-1}^{\ 2} - r_{1-2}^{\ 2}\right) - S_{g1} \tag{3}$$

$$S_2 = \pi \cdot \left(r_{2-1}^{\ 2} - r_{2-2}^{\ 2}\right) - S_{g2} \tag{4}$$

$$S_3 = \pi \cdot \left(r_{3-1}^{\ 2} - r_{3-2}^{\ 2}\right) - S_{g3} \tag{5}$$

$$S_4 = \pi \cdot \left(r_{4-1}^{\ 2} - r_{4-2}^{\ 2}\right) - S_{g4} \tag{6}$$

$$S_1 = S_2 = S_3 = S_4 \tag{7}$$

where, $r_{1\text{-}1}$ and $r_{1\text{-}2}$ are the outer ring radius and inner ring radius of the first phase ($S_1$), $r_{2\text{-}1}$ and $r_{2\text{-}2}$ are the outer ring radius and inner ring radius of the second phase ($S_2$), $r_{3\text{-}1}$ and $r_{3\text{-}2}$ are the outer ring radius and inner ring radius of the third phase ($S_3$), $r_{4\text{-}1}$ and $r_{4\text{-}2}$ are the outer ring radius and inner ring radius of the fourth phase ($S_4$), and $S_{g1}$, $S_{g2}$, $S_{g3}$, and $S_{g4}$ are the gap areas in the corresponding phase. The corresponding parameters can be calculated according to the above principle equations for the pattern design.

## Supplementary Movie:

**Movie S1**｜The temperature hygrometer is driven by the D-TENG at a rotational rate of 420 rpm.

**Movie S2**｜Four lamps rated 12W are lit by the D-TENG at a rotational rate of 420 rpm.

**Movie S3**｜1824LEDs are lit by the D-TENG at a rotational rate of 420 rpm.

# References


1. X. Li, X. Yin, Z. Zhao, L. Zhou, D. Liu, C. Zhang, C. Zhang, W. Zhang, S. Li, J. Wang and Z. L. Wang, Advanced Energy Materials, 2020, **10**, 1903024.
2. H. Ryu, J. H. Lee, U. Khan, S. S. Kwak, R. Hinchet and S.-W. Kim, Energy & Environmental Science, 2018, **11**, 2057-2063.
3. J. Wang, H. Li, D. Zhao, Q. Gao, X. Cheng, J. Wen, Z. L. Wang and T. Cheng, Advanced Materials Technologies, 2023, **n/a**, 2300480.
4. Z. Wu, S. Wang, Z. Cao, R. Ding and X. Ye, Nano Energy, 2021, **83**, 105787.
5. J. Wang, Y. Li, Z. Xie, Y. Xu, J. Zhou, T. Cheng, H. Zhao and Z. L. Wang, Advanced Energy Materials, 2020, **10**, 1904227.
6. Y. Hu, X. Li, Z. Zhao, C. Zhang, L. Zhou, Y. Li, Y. Liu, J. Wang and Z. L. Wang, Small Methods, 2021, **5**, e2100936.
7. P. Chen, J. An, R. Cheng, S. Shu, A. Berbille, T. Jiang and Z. L. Wang, Energy & Environmental Science, 2021, **14**, 4523-4532.
8. M. Li, T. Jiang, Y. Ren and H. Jiang, Nano Energy, 2022, **103**, 107777.
9. X. Li, C. Zhang, Y. Gao, Z. Zhao, Y. Hu, O. Yang, L. Liu, L. Zhou, J. Wang and Z. L. Wang, Energy & Environmental Science, 2022, **15**, 1334-1345.